INTERNATIONAL JOURNAL FOR NUMERICAL METHODS IN FLUIDS, VOL. 15, 1243–1258 (1992)

AN ORTHOGONAL MAPPING TECHNIQUE FOR THE COMPUTATION OF A VISCOUS FREE-SURFACE FLOW

K. A. CLIFFE

Harwell Laboratory, Didcot, Oxfordshire OX11 0RA, U.K.

S. J. TAVENER

Department of Mathematics, Pennsylvania State University, University Park, PA 16802, U.S.A.

AND

A. A. WHEELER

School of Mathematics, University of Bristol, Bristol BS8 1TW, U.K.

SUMMARY

In this paper we describe finite element computations of the free-surface flow of a viscous fluid down an undulating inclined plane. The technique developed here employs an orthogonal mapping that is computed along with the velocity and pressure. This is allied to a technique to compute symbolically the Jacobian and other derivatives required for numerical continuation methods. The solutions obtained are compared with laboratory experiments and finite element computations reported by Pritchard and co-workers. The finite element computational method used by these authors employs spines to represent the free surface. An excellent agreement is shown to exist between the new computations and the laboratory experiments, and with the numerical solutions of Pritchard and co-workers.

KEY WORDS Free surface Viscous flow Finite element method Orthogonal mappings

1. INTRODUCTION

In this paper we consider the free-surface flow of a Newtonian fluid down a smoothly perturbed inclined plane. The flows considered here have been posed by Pritchard, *et al.*[1] as a set of test problems for quantifying the performance of methods for solving viscous free-surface flows. Pritchard *et al.* describe the experimental apparatus and their technique for measuring free-surface profiles in the laboratory. They report quantitative comparisons between the laboratory flows and large-scale numerical computations using the FIDAP finite-element code.[2] This code uses a spine representation of the free-suface, a method which will be described briefly below. Readers interested in a full description of the experiments and the FIDAP computations are referred to Reference 1. The experiments and numerical results of Pritchard *et al.*[1] will be compared with those obtained using a different numerical technique described in detail below. This technique employs an orthogonal co-ordinate transformation of the fluid region, and is based on the ENTWIFE finite-element package.[3]

Our aim is to incorporate a co-ordinate transformation scheme within a finite element code (ENTWIFE) that is capable of performing numerical continuation and numerical computations of singularities up to co-dimension two by extended system techniques. A discussion of continuation methods can be found in Reference 4 and descriptions of extended systems for computing

Received December 1991
Revised May 1992

higher-order singularities can be found in a series of papers by Jepson and Spence[5,6] and Jepson *et al.*[7] A preprocessing technique which performs symbolic computations was used to provide the FORTRAN subroutines to evaluate the Jacobian and high-order derivatives of the non-linear discretized equations. This work represents the first non-trivial test of the synthesis of these three techniques.

Viscous free-surface problems, such as the motion of a bubble in a fluid, the dynamics of liquid bridges and menisci, and the motion of thin fluid films over inclined surfaces, provide difficult computational fluid dynamics problems which are relevant to a variety of industrial processes, such as the growth of crystals for the electronics industry, the coating of photographic films and magnetic tape, and heat transfer devices. For a review, see Reference 8.

One numerical approach to the solution of free-boundary problems is to define the free-surface by its position along a predetermined array of spines (see e.g. References 9 and 10). The vertices of the finite elements are constrained to lie on the spines, ensuring that the mesh does not become badly distorted during the iterative process. This method has been employed successfully by Scriven and co-workers[9-11] for computing coating flows. It has the disadvantage that it requires *a priori* an intelligent guess of the solution so that the spines may be arranged to capture best the shape of the free surface, or requires an elaborate remeshing procedure such as that described by Christolodou and Scriven.[11] The method will fail if the free surface becomes parallel to the spines and will be poorly conditioned if the free surface becomes nearly parallel to the spines. A study of this method and its application to the free-surface flow studied herein is presented by Pritchard *et al.*[1]

An alternative approach is to employ a co-ordinate transformation of the unknown fluid region to a known region, say the unit box or unit circle. The free-surface problem may then be posed as the following fixed-point iterative scheme. At each iteration one of the three interfacial boundary conditions (e.g. the normal-stress condition) is relaxed, the free-surface is considered fixed and the interior flow is computed on the mesh generated for the current region. The remaining boundary condition is then invoked and the associated residuals used to update the co-ordinate transformation. These two steps are then repeated until convergence. For a finite difference implementation, see References 12 and 13. Such a procedure becomes very complicated for systems in which there is more than one free surface. Further, it must often be severely under-relaxed in order to be stable and since it is fixed-point iteration, it is at best only linearly convergent. For a discussion of the properties of this method, see Reference 14.

Alternatively, the co-ordinate transformation (the mesh) and flow variables may be computed simultaneously, employing a Newton iterative technique to solve the full system of algebraic equations that arise from both the governing equations and co-ordinate transformation. For a finite difference implementation, see Reference 15. In the ENTWIFE implementation, continuation and numerical singularity techniques may be employed on the full non-linear system in order to compute both regular and, more importantly, singular points, at which the flow may change stability. Each Newton iteration is computationally more expensive than a single iteration of the fixed-point iteration, but when continuation is used to provide a good initial guess and an efficient direct frontal solver (ideally, one which takes advantage of the structure of the stiffness matrix) is employed, the quadratic convergence of the Newton scheme quickly offsets this extra expense.

For both the fixed-point or Newton schemes, the computation of the co-ordinate transformation is a key issue. The mesh must be well-distributed across the fluid region in the physical domain and, ideally, concentrated in regions where there are fine-grained flow structures. Mesh geneation is an area that has been well-studied over the last 20 years, and is the subject of many papers. It has been the subject of much research in the context of aerodynamics, in which

body-fitted meshes are required in order to compute the air flow about aerodynamic control surfaces. This area is reviewed by Eiseman[16] and Thompson.[17] Such meshes may be orthogonal or non-orthogonal, but in either case they may be computed by solving a pair of elliptic partial differential equations for the underlying co-ordinate transformation. Orthogonal meshes are desirable because they considerably simplify the governing equations to be solved in the reference domain. For example, the Laplacian operator is invariant under a conformal transformation. The complexity of the governing equations is an important issue when Newton iteration and numerical singularity techniques are to be employed since they require not only the Jacobian but also the higher-order derivatives (typically, up to third order) for the characterization of singular points. The correct encoding of these derivatives is a laborious and error-prone exercise. We used REDUCE[18] to symbolically compute the Jacobian and write the relevant FORTRAN statements required by ENTWIFE. Orthogonal transformations such as those used in this study are known to create meshes which are subject to a crowding phenomena in the vicinity of a reentrant corner and which penetrate a notch only weakly. These problems arise due to the development of a singularity in the transformation. This has been vividly demonstrated by Menikoff and Zemach[19] in the particular case of conformal mapping. This problem may be mitigated to some extent by dynamic re-gridding or re-parametrizing the transformed domain.

An alternative approach to mesh generation involves the use of algebraic mappings to define the relation between the physical space and the transformed space. Because the mapping is prescribed relatively simply, the crowding phenomena can be easily overcome, but with the disadvantage that the governing equations in the transformed domain become highly complex. Brown and co-workers[20,21] have successfully incorporated such non-orthogonal mappings within a global Newton scheme, which they have applied to the study of solidification problems.

Another way to overcome this difficulty, which is the subject of much recent research, is to construct a functional of the co-ordinate transformation, chosen such that its minimization offsets the desirable quality of orthogonality against the undesirable quality of crowding.[22] In this method the corresponding Euler–Lagrange equations are solved numerically to yield meshes that satisfactorily cover even the most distorted domains. However, in some situations the mapping equations may change from elliptic to hyperbolic type, which results in a breakdown of the method. More recently, Christodoulou and Scriven.[23] have utilized a different functional that overcomes this difficulty.

In this paper we employ an orthogonal grid transformation technique to the problem of flow down an undulating inclined surface. Our main purpose is to quantitatively compare this technique against the careful laboratory experiments and numerical computations of Pritchard *et al.*[1] We show that excellent agreement is obtained. In Section 2 we describe the physical problem and present the governing equations. In Section 3 we describe the orthogonal grid transformation technique and outline its implementation in the finite element package ENTWIFE. In the last section we present the results from this method and compare and contrast them with the results obtained by Pritchard *et al.*[1] using the FIDAP finite element package (which employs a spine representation of the free surface) and with their laboratory experiments.

2. PROBLEM DESCRIPTION AND GOVERNING EQUATIONS

We consider the flow of a viscous, incompressible, Newtonian fluid down an inclined channel of width w. There are two smooth bumps in the bed of the channel which extend across the width of the channel perpendicular to the side walls. We assume that this flow is essentially two-dimensional and define a Cartesian co-ordinate system rotated to be coincident with the mean slope of the inclined plane ($\sim 4{\cdot}22^\circ$ to the horizontal in the experimental situation). Let Ω denote

the flow domain with boundary $\partial\Omega$. We divide the boundary $\partial\Omega$ into four disjoint parts, $\partial\Omega = \Gamma_U \cup \Gamma_B \cup \Gamma_D \cup \Gamma_F$, where Γ_U is the upstream end of our flow domain and is given by $x=0$, Γ_B is the sloping surface of the perturbed inclined plane, which we describe by a known smooth function $y=b(x)$, Γ_D is the downstream end of the flow domain and is given by $x=L$, and Γ_F is the free surface of the fluid. Abergel and Bona[24] show that the free-surface flow in this domain approaches the Poiseuille–Nusselt flow down an inclined plane exponentially, both upstream and downstream of the localized bump region.

Let H be the height of this asymptotic flow which is determined from the volume flow rate per unit width Q, as $(3Qv/g\sin\alpha)^{1/3}$, where v is the kinematic viscosity of the fluid, g is the acceleration due to gravity and α is the slope of the reference plane. We shall use the length scale H to characterize Ω and $U=Q/H$ to scale the velocity field. The dynamical equations governing the steady fluid motions in Ω are

$$R(\mathbf{u}\cdot\nabla)\mathbf{u} = \nabla\cdot\boldsymbol{\sigma} - G\mathbf{j}, \tag{1}$$

and

$$\operatorname{div}\mathbf{u} = 0, \tag{2}$$

where $\mathbf{u}(\mathbf{x})$ is the velocity at $\mathbf{x}\in\Omega$, $\mathbf{j}$ is the unit vector directed vertically upwards, $R=UH/v$ $(=Q/v)$ is the Reynolds number and $G=gH^2/vU$. The stress tensor $\boldsymbol{\sigma}(\mathbf{x})$, which is scaled by $\rho vU/H$, where ρ is the fluid density, is given in Cartesian co-ordinates by

$$\sigma_{ij} = -p\delta_{ij} + (u_{i,j} + u_{j,i}), \tag{3}$$

where $p(\mathbf{x})$ is the pressure at $\mathbf{x}\in\Omega$. For $\mathbf{x}\in\Gamma_U$ and $\mathbf{x}\in\Gamma_D$ we impose the Dirichlet conditions

$$\mathbf{u}(\mathbf{x}) = \mathbf{g}_p(\mathbf{x}), \tag{4}$$

where $\mathbf{g}_p(x) = [\frac{3}{2}y(2-y), 0]$ is the far-field Poiseuille flow. For $\mathbf{x}\in\Gamma_B$ we impose the no-slip condition

$$\mathbf{u}(\mathbf{x}) = \mathbf{0}. \tag{5}$$

On the free surface $\mathbf{x}\in\Gamma_F$, we impose a kinematical constraint which, for steady flows, is that the velocity field at the free surface be tangential to the surface itself, i.e.

$$\mathbf{u}(\mathbf{x})\cdot\mathbf{n} = 0, \tag{6}$$

where $\mathbf{n}$ is the local (outward) normal to the surface. The normal stress along Γ_F must be balanced by surface tension effects as

$$\sigma_{ij}n_j = n_i \frac{T}{\rho vU}\kappa, \tag{7}$$

where κ is the curvature of the surface, reckoned positive when the radius of curvature is directed into Ω, and T is the surface tension. We shall define the non-dimensional surface tension parameter as $S=T/\rho vU$. Further, we need to ensure that the tangential stress at the free surface is zero, i.e. for $\mathbf{x}\in\Gamma_F$

$$\sigma_{ij}t_i = 0. \tag{8}$$

This arises as the natural boundary condition upon integrating the weak form of the Navier–Stokes equations by parts if the stress divergence form is employed (see e.g. Reference 25, p. 61).

3. ORTHOGONAL MAPPING METHOD

In this section we develop an orthogonal mapping technique to solve the free-boundary problem described in the previous section. The idea is to construct an orthogonal mapping $[\psi(x, y), \phi(x, y)]$ from the four-sided physical domain Ω, onto the unit square in the transformed domain Ω', such that the level curves of $\psi(x, y)$ and $\phi(x, y)$ are everywhere orthogonal, and the boundaries Γ_U, Γ_B, Γ_D and Γ_F are mapped onto the sides of the unit square, $\psi=0$, $\phi=0$, $\psi=1$ and $\phi=1$, respectively. The system of partial differential equations and the associated boundary conditions governing the behaviour in the physical domain are then recast with ψ and ϕ as the independent variables. The construction of an orthogonal transformation of a known fixed domain may be achieved in some cases by a conformal mapping, e.g. the use of the Schwarz–Christoffel mapping of a polygon. However, such a procedure does not, in general, permit the boundaries of a four-sided region to be mapped onto the corresponding boundaries of the unit square Ω'. The governing equations are, therefore, supplemented with additional partial differential equations and boundary conditions describing the orthogonal transformation, i.e. relating the Cartesian co-ordinates (x, y) to ψ and ϕ, and this combined system is then solved using a conventional finite element approach. As discussed in Section 1, there exists a considerable literature on boundary-fitted co-ordinate schemes. We have chosen the simplest of these, solving the generalized Cauchy–Riemann equations for the mapping. Local mesh refinement is achieved by 'patching' subdomains, defined on the reference domain, together as required. We derive the mapping equations in what we hope is a straightforward manner, based on our requirement of orthogonality. Necessarily, we have obtained the same mapping equations as presented previously by a number of authors (e.g. Reference 12).

To proceed, we first impose the condition that the co-ordinate transformation be orthogonal, in which case

$$\nabla\psi \cdot \nabla\phi = 0 \quad \text{for all } (x, y) \in \Omega, \tag{9}$$

which has the general solution

$$\psi_x = \lambda\phi_y, \tag{10}$$

$$\psi_y = -\lambda\phi_x, \tag{11}$$

where λ depends on (x, y) [or, equivalently, (ψ, ϕ)]. We now exchange the independent and dependent variables, making use of the following results:

$$\psi_x = J^{-1}y_\phi, \qquad \psi_y = -J^{-1}x_\phi, \qquad \phi_x = -J^{-1}y_\psi, \qquad \phi_y = J^{-1}x_\psi, \tag{12}$$

where

$$J = \frac{\partial(x, y)}{\partial(\psi, \phi)} \tag{13}$$

is the Jacobian of the transformation, in order to obtain

$$y_\phi = \lambda x_\psi, \tag{14}$$

$$x_\phi = -\lambda y_\psi. \tag{15}$$

These may be rearranged to give

$$\left(\frac{x_\phi}{\lambda}\right)_\phi + (\lambda x_\psi)_\psi = 0, \tag{16}$$

$$\left(\frac{y_\phi}{\lambda}\right)_\phi + (\lambda y_\psi)_\psi = 0, \tag{17}$$

which provide two elliptic partial differential equations for (x, y) on Ω', given λ. We require that λ takes a constant value in Ω' and achieve this by solving

$$\nabla^2\lambda(\psi, \phi)=0 \qquad \text{for all } (\psi, \phi)\in\Omega', \tag{18}$$

with boundary conditions

$$\frac{\partial\lambda}{\partial\mathbf{n}}=0 \qquad \text{for } (\psi, \phi)\in\delta\Omega'. \tag{19}$$

We determine the constant value by invoking the orthogonality conditions (14) and (15) at the centre of the transformed domain Ω', i.e.

$$y_\phi+x_\phi=\lambda(x_\psi-y_\psi) \quad \text{at } (\psi, \phi)=(\tfrac{1}{2}, \tfrac{1}{2}). \tag{20}$$

The sum of equations (14) and (15) is used to ensure that equation (20) is not singular when x_ψ or y_ψ is zero. We note that alternative ways of specifying the function λ are possible (see, for example, References 26–28 and 12) and that our procedure may not be the most efficient. It was chosen so that the mapping equations could be treated as simply another pair of partial differential equations to be discretized and solved using our finite element routines, thus avoiding the need to treat these equations in a special manner.

The boundary conditions on $x(\psi, \phi)$ and $y(\psi, \phi)$ are derived from the shape of the fixed boundaries of the computational domain Ω, by requiring orthogonality at the boundaries, and from the kinematic boundary condition along the free surface. For equations (16) and (17) they are, respectively,

$$x=0, \qquad y_\psi=0 \qquad \text{on } \psi=0, \tag{21}$$

$$x_\phi=-\lambda y_\psi, \qquad y=b(x) \quad \text{on } \phi=0, \tag{22}$$

$$x=L, \qquad y_\psi=0 \qquad \text{on } \psi=1, \tag{23}$$

$$x_\phi=-\lambda y_\psi, \qquad -uy_\psi+vx_\psi=0 \qquad \text{on } \phi=1. \tag{24}$$

Finally, we pin the upstream and downstream free-surface positions by imposing

$$y=1 \quad \text{at } (\psi, \phi)=(0, 1) \text{ and } (1, 1). \tag{25}$$

Thus, we are required to solve the Navier–Stokes equations (1) and (2) along with the transformation equations (16)–(18) for $\mathbf{u}$, p, x, y and λ subject to boundary conditions (4), (5), (7) and (8) on the flow variabls and (19)–(25) on the transformation.

Certain aspects of how best to impose boundary conditions for free-surface problems remain open mathematical issues (see e.g. Reference 29). Since we impose both the free-surface height and the velocity components at the upstream and downstream boundaries, the kinematic boundary condition will not be satisfied there unless the free-surface upstream and downstream is flat. (Pritchard *et al.*[29] suggest imposing a tangential velocity at both boundaries of arbitrary shape and of a size required to satisfy the kinematic condition.) Fortunately, such an incompatibility never arose. Abegel and Bona[24] show that, exponentially, the flow approaches one in which the free surface is parallel to the bed; and the computations were observed to be robust with minor variations in the position of the upstream and downstream boundaries. Moreover, the comparisons reported in the next section suggest that our choices of these and other boundary conditions are satisfactory.

A weak form of the above system of partial differential equations is obtained by applying the standard Galerkin approach. In view of the free-surface conditions (7) and (8), we have expressed the viscous contribution to the momentum equation (1) in the form given by (3). The natural boundary condition arising in the resulting weak formulation is the prescription of the shear stress on the boundary (see Reference 25, p. 61). The weak form of the momentum equations developed below has been derived previously by both Ruschak[30] and Kruyt *et al.*[31]

First, for the transformation variables $x(\psi, \phi)$, $y(\psi, \phi)$ and $\lambda(\psi, \phi)$ we have

$$\int_{\Omega'} (\lambda x_\psi \xi_{1,\psi} + \lambda^{-1} x_\phi \xi_{1,\phi})\, d\psi\, d\phi - \int_{\phi=0} \xi_1 y_\psi\, d\psi + \int_{\phi=1} \xi_1 y_\psi\, d\psi = 0, \tag{26}$$

$$\int_{\Omega'} (\lambda y_\psi \xi_{2,\psi} + \lambda^{-1} y_\phi \xi_{2,\phi})\, d\psi\, d\phi + \int_{\phi=1} (-u y_\psi + v x_\psi)\xi_2\, d\psi = 0, \tag{27}$$

$$\int_{\Omega'} (\lambda_\psi \chi_\psi + \lambda_\phi \chi_\phi)\, d\psi\, d\phi = 0, \tag{28}$$

where $\xi_1(\psi, \phi)$, $\xi_2(\psi, \phi)$ and $\chi(\psi, \phi)$ are suitable test functions for $x(\psi, \phi)$, $y(\psi, \phi)$ and $\lambda(\psi, \phi)$, respectively. For the velocity field $\mathbf{u}[x(\psi, \phi), y(\psi, \phi)]$, we have

$$\int_\Omega Ru_j \frac{\partial u_i}{\partial x_j} \zeta_i\, d\Omega = \int_\Omega \frac{\partial \sigma_{ij}}{\partial x_j} \zeta_i\, d\Omega - \int_\Omega (G\mathbf{j})_i \zeta_i\, d\Omega,$$

where $\zeta_1[x(\psi, \phi), y(\psi, \phi)]$ and $\zeta_2[x(\psi, \phi), y(\psi, \phi)]$ are suitable test functions for the velocity components $u[x(\psi, \phi), y(\psi, \phi)]$ and $v[x(\psi, \phi), y(\psi, \phi)]$, respectively. We use the definition of the stress tensor [equation (3)] and integrate by parts. Boundary conditions (4) and (5) require that both velocity test functions ζ_i, $i = 1, 2$ be zero on Γ_U, Γ_D and Γ_B. Using equations (7) and (8) along Γ_F we have

$$\int_\Omega Ru_j \frac{\partial u_i}{\partial x_j} \zeta_i\, d\Omega = \int_{\Gamma_F} S\kappa n_i \zeta_i\, ds - \int_\Omega \sigma_{ij} \frac{\partial \zeta_i}{\partial x_j}\, d\Omega - \int_\Omega (G\mathbf{j})_i \zeta_i\, d\Omega.$$

Since

$$\kappa n_i = \frac{dr_i}{ds},$$

we have

$$\int_\Omega Ru_j \frac{\partial u_i}{\partial x_j} \zeta_i\, d\Omega = \int_{\Gamma_F} S \frac{dr_i}{ds} \zeta_i\, ds - \int_\Omega \sigma_{ij} \frac{\partial \zeta_i}{\partial x_j}\, d\Omega - \int_\Omega (G\mathbf{j})_i \zeta_i\, d\Omega.$$

Integrating by parts and noting that the basis functions for the both velocity components vanish at the two ends of the free surface,

$$\int_\Omega Ru_j \frac{\partial u_i}{\partial x_j} \zeta_i\, d\Omega = -\int_{\Gamma_F} Sr_i \frac{\partial \zeta_i}{ds}\, ds - \int_\Omega \left[-p \frac{\partial \zeta_j}{\partial x_j} + (u_{i,j} + u_{j,i}) \frac{\partial \zeta_i}{\partial x_j} \right] d\Omega - \int_\Omega (G\mathbf{j})_i \zeta_i\, d\Omega.$$

In terms of integrals over the transformed domain,

$$\int_{\Omega'} \left[Ru_j \frac{\partial u_i}{\partial x_j} \zeta_i - p \frac{\partial \zeta_j}{\partial x_j} + (u_{i,j} + u_{j,i}) \frac{\partial \zeta_i}{\partial x_j} + (G\mathbf{j})_i \zeta_i \right] J\, d\psi\, d\phi + \int_{\phi=1} S \frac{1}{\sqrt{(x_\psi)^2 + (y_\psi)^2}} (x_\psi \zeta_1 + y_\psi \zeta_2)\, d\psi = 0, \tag{29}$$

where the expressions appearing in the first integrand must, of course, be written in terms of the independent variables (ψ, ϕ). These are complicated expressions and are not given here. The weak form of the continuity equation, used to solve for the pressure field, is

$$\int_{\Omega'} [(u_\psi y_\phi - u_\phi y_\psi) + (v_\psi x_\phi - v_\phi x_\psi)] q \, d\psi \, d\phi = 0, \tag{30}$$

where $q(\psi, \phi)$ is a suitable test function for the pressure. The remaining boundary conditions are Dirichlet and were implemented by 'overwriting the boundary conditions' in the standard way.

A finite element discretization was used to solve the above weak formulation. The computations were performed using rectangular elements with biquadratic basis functions for the velocity field $\mathbf{u}(\psi, \phi)$, the co-ordinates $x(\psi, \phi)$ and $y(\psi, \phi)$, and for $\lambda(\psi, \phi)$. Discontinuous piecewise linear basis functions were used for the pressure. The resulting non-linear algebraic system was solved using Newton iteration. The Jacobian required by this procedure is complicated, due in part to the introduction of the co-ordinate transformation. We, therefore, developed a preprocessing package which employed the REDUCE[18] algebraic manipulation language to compute symbolically the elements of the Jocobian and write the necessary FORTRAN statements required by ENTWIFE. This proved to be essential to encode accurately the Jacobian.

4. RESULTS

The orthogonal mapping technique was first tested on a viscous flow problem in a fixed domain. The flow in a slowly expanding duct was computed using the new mapping technique and compared to the results of a series of benchmark computations with the ENTWIFE code using standard grid techniques.[32]

The free-surface flow down a perturbed inclined plane described in Section 2 was computed using the orthogonal mapping and the finite element techniques discussed in Section 3. A section of the orthogonal mesh of the $Re = 25{\cdot}5$ computation is shown in Figure 1. For the purposes of illustration, the mesh has been halved in the downstream direction. The result of patching of subdomains in the reference domain to obtain local refinement is evident. Note, however, that λ is constant over the entire mesh and is normalized using equation (20) at just one point. The corresponding velocity field is shown in Figure 2. Again, only half the number of the computed

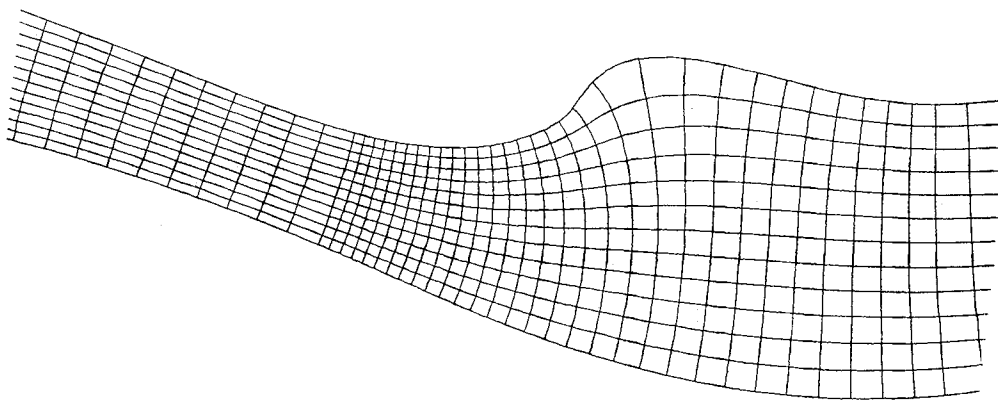

Figure 1. Orthogonal mesh downstream of first bump for $Re = 25{\cdot}5$

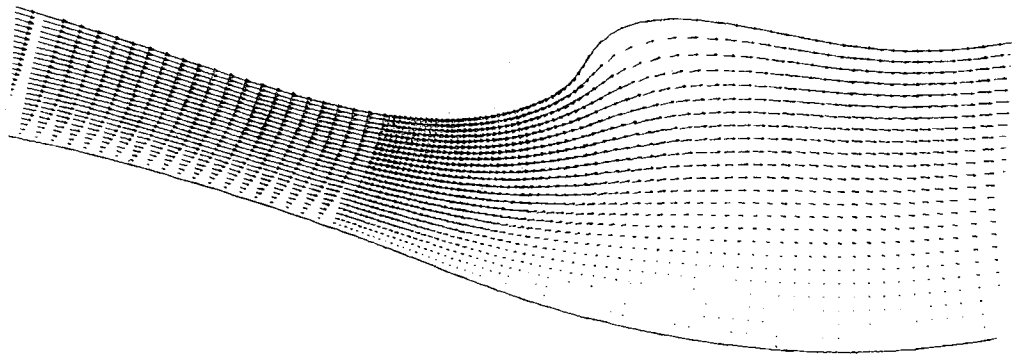

Figure 2. Velocity field downstream of first bump for Re = 25·5 computed by ENTWIFE

velocity vectors are shown. Note that the kinematic boundary condition is accurately satisfied even in this highly distorted region.

Consistent with the experience of Pritchard *et al.*[1], the region of convergence of the Newton iteration was found to be very small and care was needed to find a sufficiently accurate initial guess for the Newton iteration of converge. Numerical continuation (see. e.g. Reference 4), both with respect to the Reynolds number and with respect to the height of the bumps, was performed in order to find solutions. At larger Reynolds numbers, fairly small steps were necessary to ensure convergence. For example, at a Reynolds number of 25·5, the bed height was increased from zero to its full height in 20 discrete steps. Given a sufficiently accurate initial guess, the ultimately quadratic convergence of Newton's method was always observed.

The position of the free surface computed by this method was compared with the experimental measurements and FIDAP computations reported by Prichard *et al.*[1] The experimental measurements and the two finite element solutions are shown in Figures 3–6 for four different flow rates. Further details of the $Re = 20{\cdot}5$ flow are shown in Figures 7 and 8. The norms reported in Table I are for the solution on a mesh with 250 elements in the downstream direction and 12 elements in the cross-stream direction.

The computations using the finite element code FIDAP employed Taylor–Hood triangular elements with biquadratic velocity and continuous linear pressure interpolation. Continuation in the height of the bumps was used to find a solution for a small Reynolds number flow. The other flows were then found by continuation in the Reynolds number. The norms reported in Table I are for the solution on a mesh with 332 elements in the downstream direction and 16 elements in the cross-stream direction. By comparing this solution with a solution computed on a mesh with 664×64 elements, it is believed that the solution on the 332×32 element mesh has converged to within 1%. A half-parabolic Poiseuille flow was applied at the upstream and downstream boundaries, where the depth of the flow was fixed. The velocity field at the element vertices for the $Re = 25{\cdot}5$ FIDAP computation is plotted in Figure 9, where it can be observed that the spine technique has problems satisfying the kinematic boundary condition in regions where the angle between the spines and the free surface becomes 'small'. It should be noted, however, that the elements are isoparameteric and the approximation to the free surface is piecewise quadratic rather than piecewise linear as plotted; hence, the situation is not as bad as it appears from the figure.

The pairwise differences between each of the three free-surface approximations are tabulated in Table I. The free-surface positions are compared at the downstream locations at which the

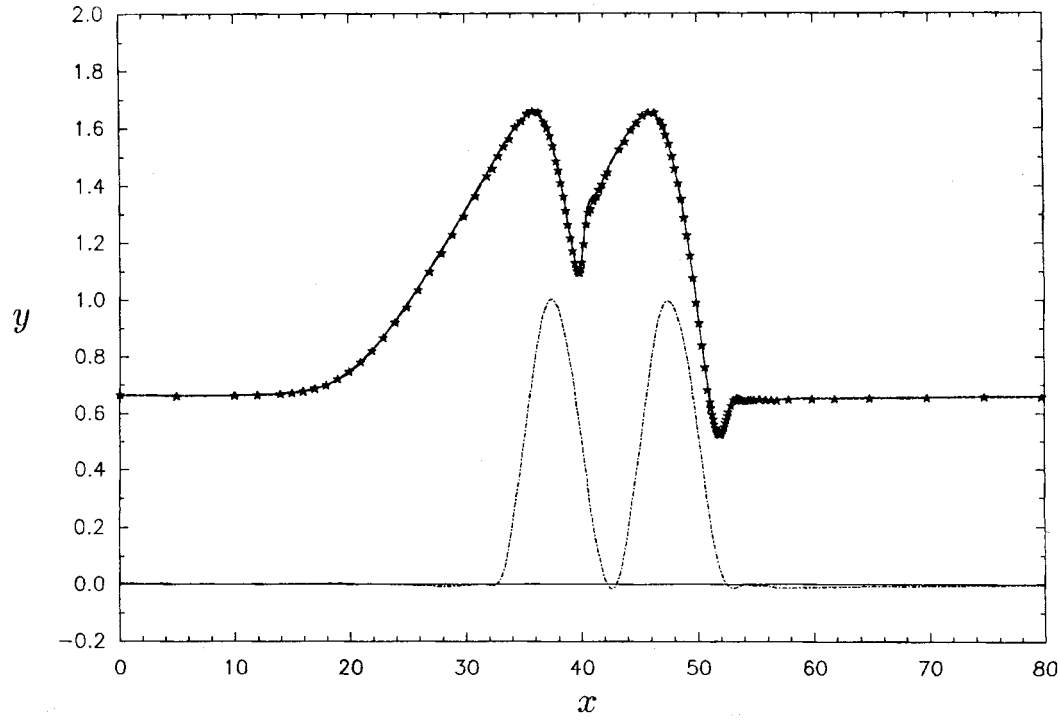

Figure 3. Comparison of experimental, FIDAP and ENTWIFE free-surface positions for $Re=12{\cdot}2$, $S=3{\cdot}38$ and $H=0{\cdot}660$: ⋆ experimental observation; --- FIDAP computation; —— ENTWIFE computation. The chained line represents the bed, and the solid base line the reference plane

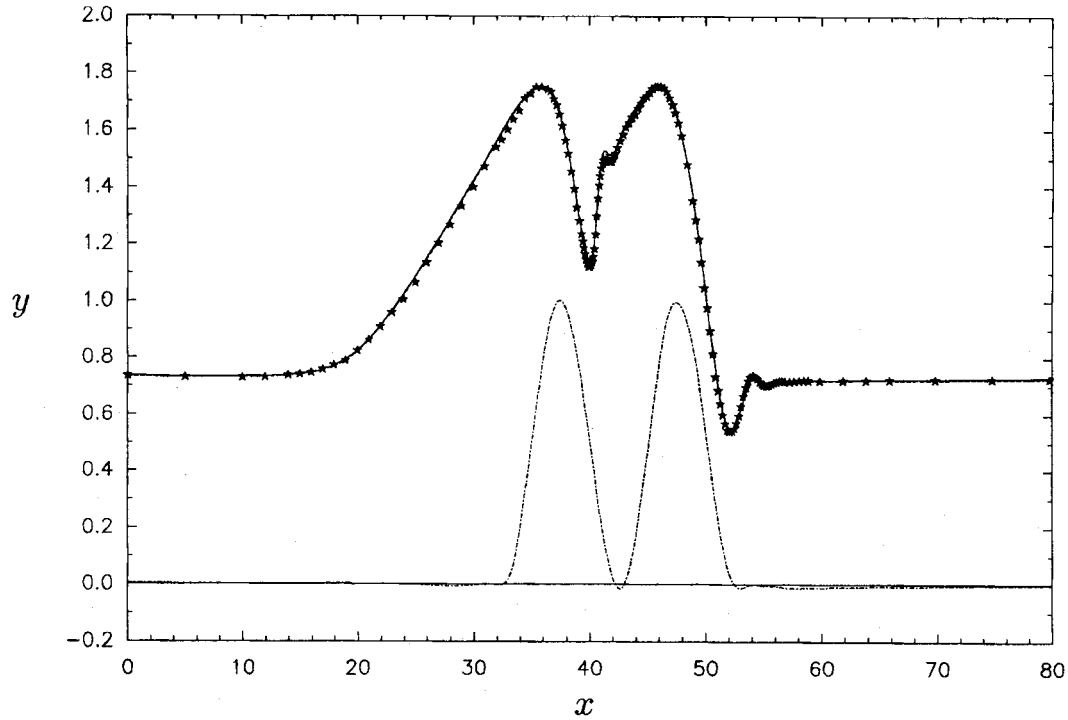

Figure 4. Comparison of experimental, FIDAP and ENTWIFE free-surface positions for $Re=16{\cdot}2$, $S=2{\cdot}77$ and $H=0{\cdot}729$: ⋆ experimental observation; --- FIDAP[1] computation; —— ENTWIFE computation. The chained line represents the bed, and the solid base line the reference plane

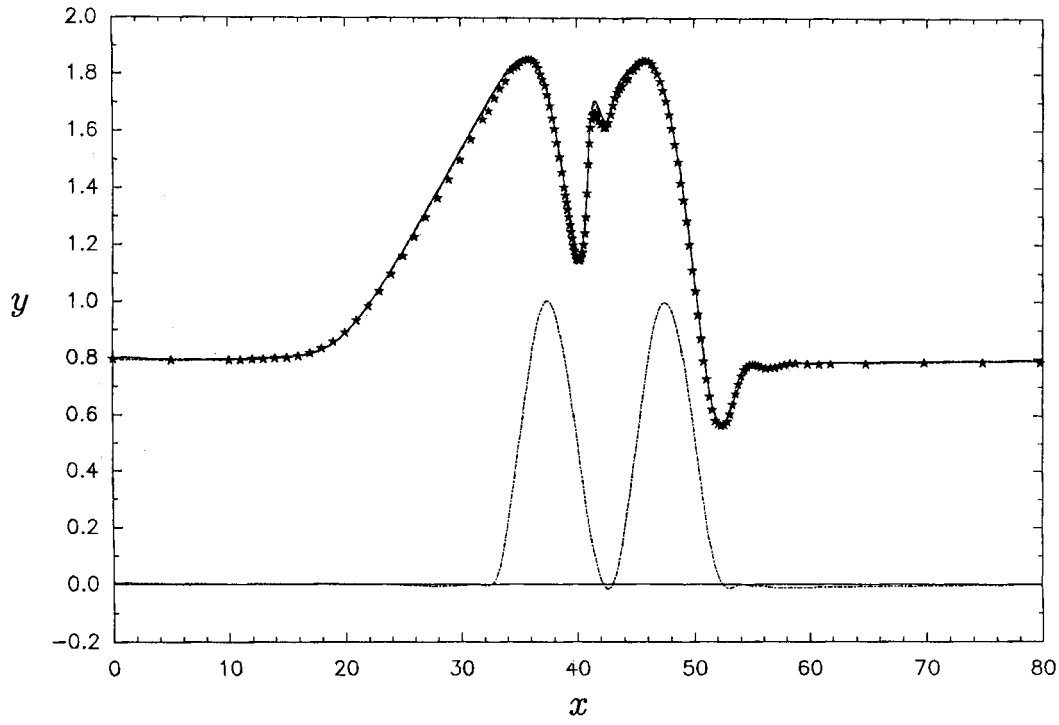

Figure 5. Comparison of experimental, FIDAP and ENTWIFE free-surface positions for $Re=20{\cdot}5$, $S=2{\cdot}36$ and $H=0{\cdot}792$: • experimental observation; --- FIDAP[1] computation; —— ENTWIFE computation. The chained line represents the bed, and the solid base line the reference plane

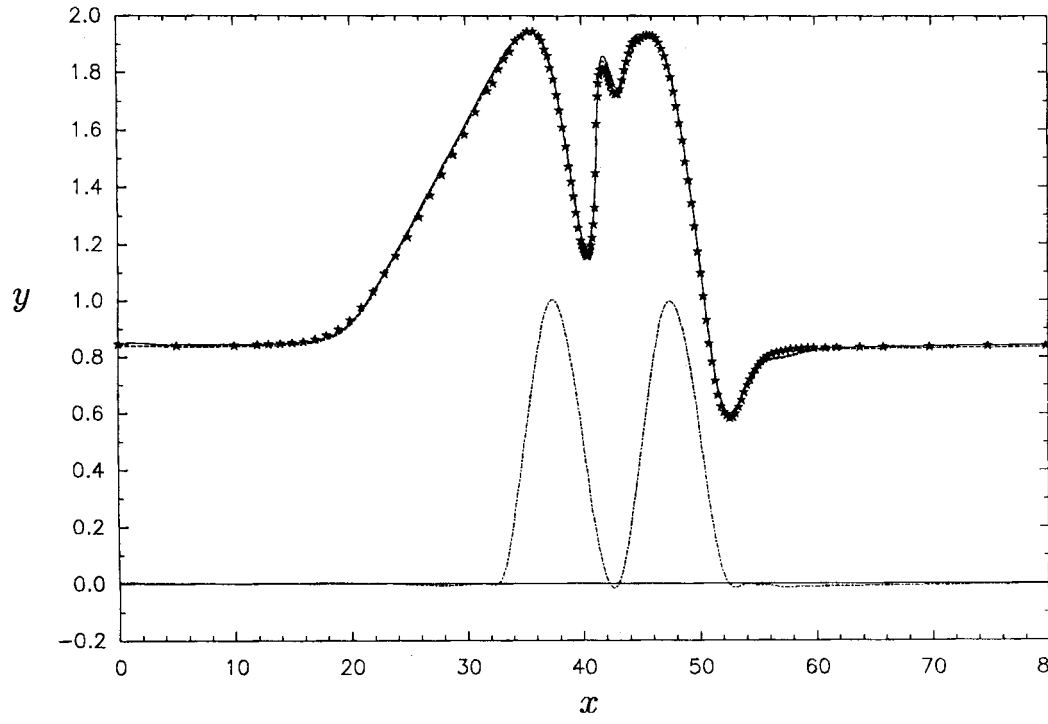

Figure 6. Comparison of experimental, FIDAP and ENTWIFE free-surface positions for $Re=25{\cdot}5$, $S=2{\cdot}08$ and $H=0{\cdot}840$: ⋆ experimental observation; --- FIDAP[1] computation; —— ENTWIFE computation. The chained line represents the bed, and the solid base line the reference plane

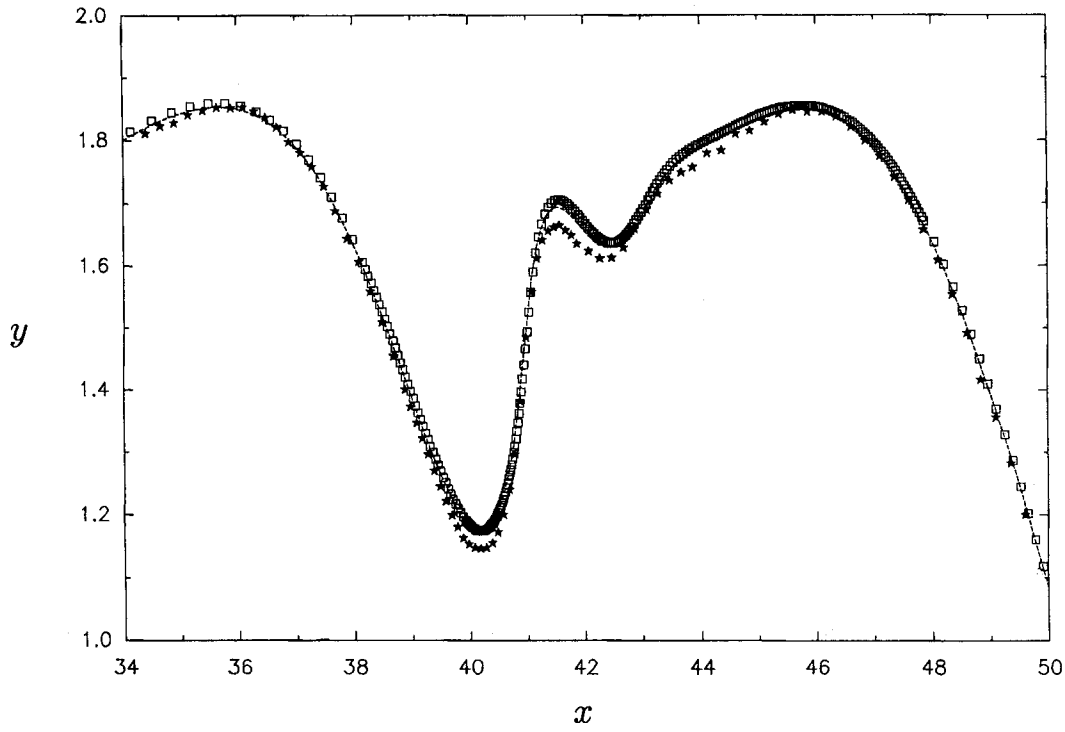

Figure 7. Details of the $Re = 20{\cdot}5$ experimental FIDAP and ENTWIFE free-surface comparison between downstream locations 34 and 50: ⋆ experimental observations; – – – FIDAP[1] computation; □ ENTWIFE computation

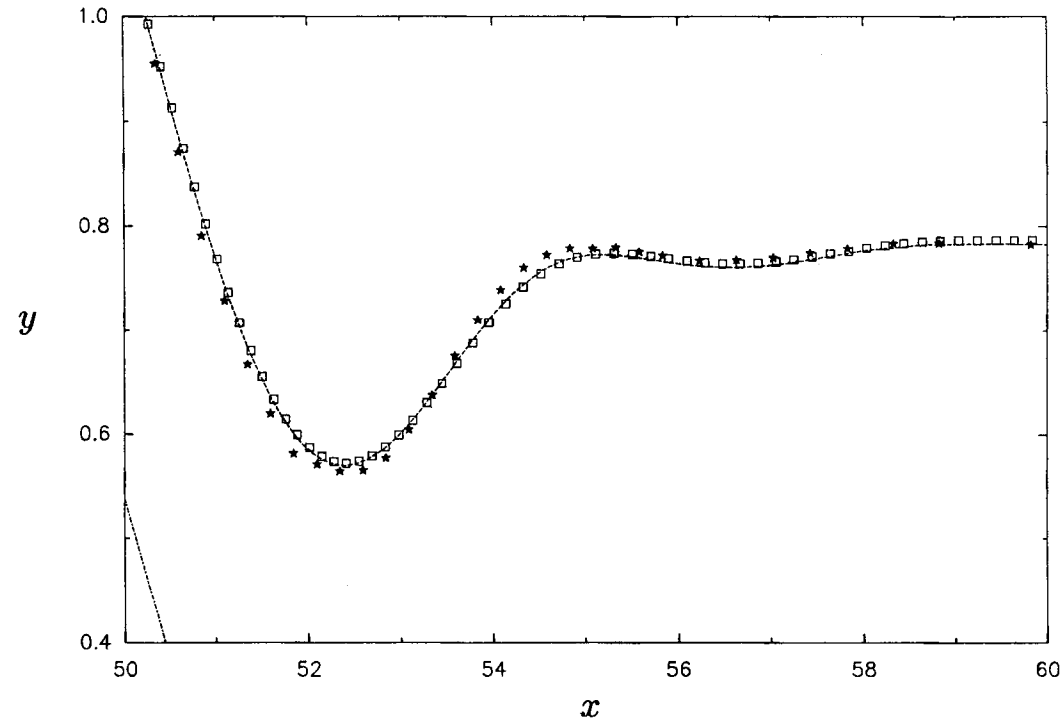

Figure 8. Details of the $Re = 20{\cdot}5$ experimental, FIDAP and ENTWIFE free-surface comparison between downstream locations 50 and 60: ⋆ experimental observations; – – – FIDAP[1] computation; □ ENTWIFE computation. The chained line represents the bed

Table I. Comparisons of experimental, FIDAP and ENTWIFE free-surface positions

	l_1	l_2	l_∞
$Re = 12{\cdot}2$, $S = 3.38$, ne = 125			
ENTWIFE versus experiment	0·022	0·017	0·038
FIDAP* versus experiment	0·013	0·013	0·032
ENTWIFE versus FIDAP	0·014	0·0086	0·0065
$Re = 16{\cdot}2$, $S = 2{\cdot}77$, ne = 147			
ENTWIFE versus experiment	0·026	0·022	0·034
FIDAP* versus experiment	0·019	0·017	0·029
ENTWIFE versus FIDAP	0·014	0·0087	0·0095
$Re = 20{\cdot}2$, $S = 2{\cdot}36$, ne = 153			
ENTWIFE versus experiments	0·036	0·029	0·046
FIDAP* versus experiments	0·026	0·023	0·032
ENTWIFE versus FIDAP	0·014	0·0096	0·020
$Re = 25{\cdot}5$, $S = 2{\cdot}08$, ne = 146			
ENTWIFE versus experiments	0·033	0·029	0·083
FIDAP* versus experiments	0·033	0·024	0·050
ENTWIFE versus FIDAP	0·025	0·0016	0·034

* The results of all FIDAP computations are reported with the permission of Pritchard *et al.*[1]

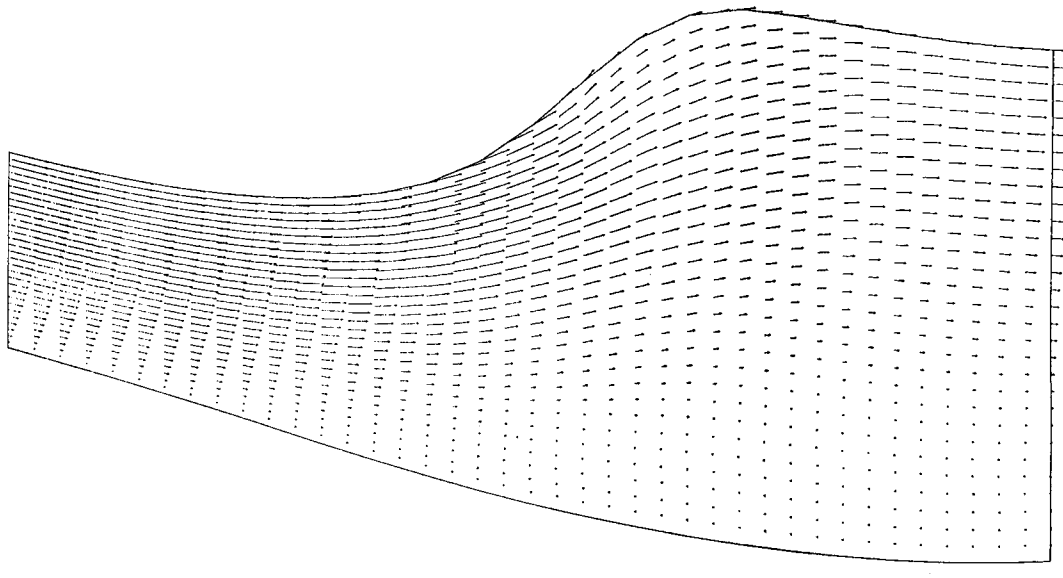

Figure 9. Velocity field flow downstream of first bump for $Re = 25{\cdot}5$ computed using FIDAP[1]

experimental measurements were made and the different norms are defined as

$$l_p=\left[\sum_{i=1}^{ne}\left(w_i\frac{h_{2i}-h_{1i}}{h_{2i}-H}\right)^p\right]^{1/p},$$

where ne is the number of experimental measurements, h_{2i}, h_{1i} are the heights of the free surface above the reference plane at downstream location x_i, H is the asymptotic height of the free surface, measured far upstream (or downstream) of the bumps, and $w_i=0{\cdot}5(x_{i+1}-x_{i-1})$.

The l_2 error between the computations and the experiments is seen to be less than 3% in all cases. The l_2 difference between the computations is less than 2% for all Reynolds numbers and less than 1% for Reynolds numbers below 20·5. In all four cases the maximum discrepancy between the three different free-surface positions occurs where the free-surface height increases rapidly after its minimum value between the two bumps. The site of the large maximum error for the $Re=25{\cdot}5$ flow is shown in Figure 10. For this flow, the maximum difference between all three pairs of free-surface approximations occurs at a downstream location of $x=41{\cdot}28$.

At Reynolds number 25·5, both computational methods predict a similar structure downstream of the second bump that differs qualitatively from that which is observed in the experiments. This difference is illustrated in Figure 11. For this and larger Reynolds number flows, definite three-dimensional structures were observed in the laboratory experiments by Pritchard *et al.*[1] and the validity of comparing the results of two-dimensional computations with those of experiments is increasingly doubtful.

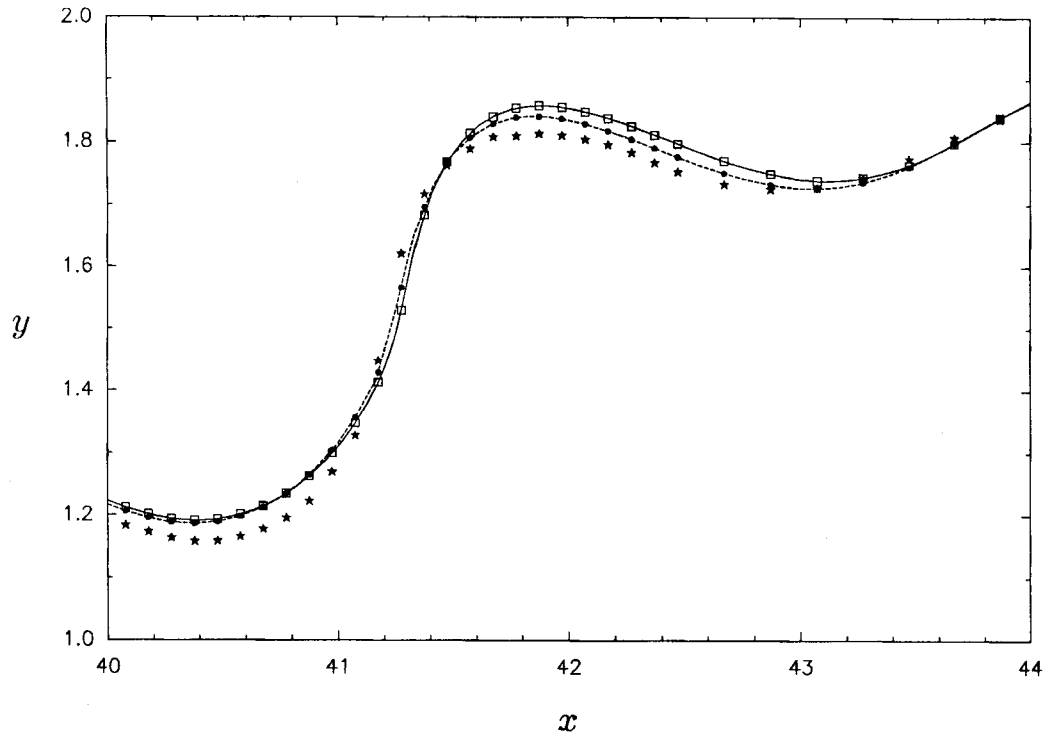

Figure 10. Location of maximum error for $Re=25{\cdot}5$: • experimental observation; • FIDAP[1] computation; □ ENTWIFE computation

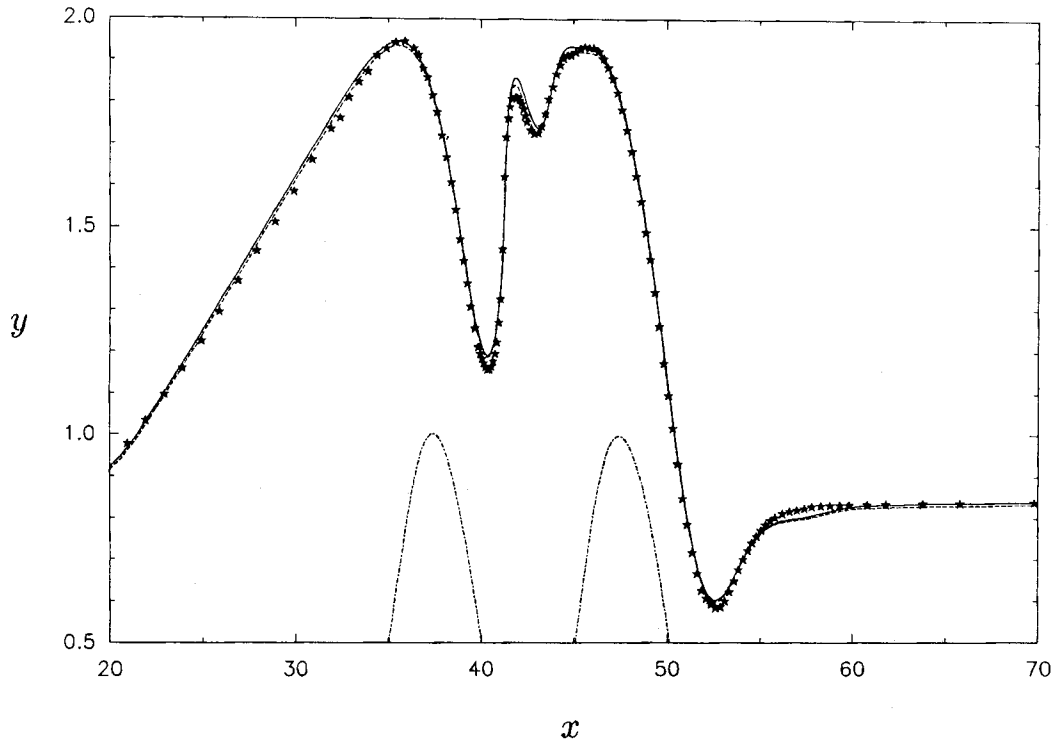

Figure 11. Qualitatively different behaviour between computed and experimental free-surface positions downstream of the second bump for $Re = 25{\cdot}5$: ⋆ experimental observation; --- FIDAP[1] computation; —— ENTWIFE computation. The chained line represents the bed

5. CONCLUSIONS

We have embedded an orthogonal mapping technique into a general-purpose finite element package and successfully computed a class of viscous free-surface flows. Comparisons against the laboratory experiments and FIDAP computations of Pritchard *et al.*[1] are within 3% and 2%, respectively, in the l_2 norm we have defined. At Reynolds numbers less than 25, the computations are within 1% of each other. The orthogonal mapping approach allows an accurate representation of the velocity field to be determined in areas of high curvature with greater ease than using the spine technique. Further, the use of a symbolic manipulation package such as REDUCE has allowed the automatic construction of subroutines to evaluate the higher-order derivatives required for computations of singular points by extended system techniques. The numerical bifurcation potential of ENTWIFE in the context of free-surface flows is presently being explored.

ACKNOWLEDGEMENTS

Two of the authors, K. A. C. & A. A. W., acknowledge the support from the Corporate Research Programme of A. E. A. Technology; S. J. T. was supported in part by the National Science Foundation through award number DMS 8805311-04.

REFERENCES

1. W. G. Pritchard, L. R. Scott and S. J. Tavener, 'Viscous free-surface flow over a perturbed inclined plane', *Phil. Trans. Roy. Soc. Lond.* (1992) (to appear).
2. M. S. Engelman, 'FIDAP—A fluid dynamics analysis package', *Adv. Eng. Software*, **4**, 163 (1982).
3. ENTWIFE Fluid Dynamics Analysis Package, A.E.A. Harwell Laboratory, Oxfordshire.
4. H. B. Keller, 'Numerical solution of bifurcation and nonlinear eigenvalue problems, in P. H. Rabinowitz (ed.), *Applications of Bifurcation Theory*, Academic Press London, p. 359, 1977.
5. A. D. Jepson and A. Spence, 'Folds in solutions of two parameter systems and their calculations. Part I', *SIAM J. Numer. Anal.*, **22**, 347 (1985).
6. A. D. Jepson and A. Spence, 'The numerical solution of nonlinear equations having several parameters I: scalar equations', *SIAM J. Numer. Anal.*, **22**, 736 (1985).
7. A. D. Jepson, A. Spence and K. A. Cliffe, 'The numerical solution of nonlinear equations having several parameters III: equations with Z_2-Symmetry, *SIAM J. Numer. Anal.*, **28**, 809 (1991).
8. K. J. Ruschak, 'Coating flows', *Ann. Rev. Fluid Mech.*, **17**, 65 (1985).
9. S. F. Kistler and L. E. Scriven, 'Coating flow theory by finite element and asymptotic analysis of the Navier–Stokes system,' *Int. j. numer. methods fluids*, **4**, 207 (1984).
10. H. Saito and S. E. Scriven, 'Study of coating flow by the finite element method', *J Comput. Phys.* **42**, 53 (1981).
11. K. N. Christolodou and L. E. Scriven, 'The fluid mechanics of slide coating', *J. Fluid Mech.*, **208**, 321 (1989).
12. G. Riskin and L. G. Leal, 'Orthogonal mapping', *J. Comput. Phys.*, **50**, 71 (1983).
13. G. Riskin, and L. G. Leal 'Numerical solution of free-boundary problems in fluid mechanics', *J. Fluid Mech.*, **148**, 1 (1984).
14. D. S. Dandy and L. G. Leal, 'Bouyancy-driven motion of a deformable drop through a quiescent liquid at intermediate Reynolds numbers', *J. Fluid Mech.*, **208**, 161 (1989).
15. D. S. Dandy and L. G. Leal 'A Newton's method scheme for solving free-surface flow problems', *Int. j. numer. methods fluids*, **9**, 1469 (1989).
16. P. R. Eiseman, 'Grid generation for fluid mechanics computations', *Ann. Rev. Fluid Mech.*, **17**, 487 (1985).
17. J. F. Thompson, *Numerical Grid Generation*, North-Holland, New York, 1982.
18. A. C. Hearn, '*REDUCE users manual*, Rand Publication CP78, Santa Monica, CA, 1987.
19. R. Menikoff and C. J. Zemach, 'Methods for numerical conformal mapping', *J. Comput. Phys.*, **36**, 366 (1980).
20. H. M. Ettouney and R. A. Brown, 'Finite-element methods or steady solidification problem', *J. Comput. Phys.*, **49**, 118 (1983).
21. L. H. Ungar, N. Ramprasad and R. A. Brown, 'Finite element methods for unsteady solidification problems arising in prediction of morphological structures', *J. Sci. Comput.*, **3**, 77 (1988).
22. J. U. Brackbill and J. S. Saltzmann, 'Adaptive zoning for singular problems in two dimensions', *J. Comput. Phys.*, **46**, 342 (1982).
23. K. N. Christolodou and L. E. Scriven, 'Discretization of free surface flows and other moving boundary problems', *J. Comp. Phys.*, **99**, 39 (1992).
24. F. Abergel and J. L. Bona, 'A mathematical theory for viscous, free-surface flow over a perturbed inclined plane', *Arch. Rat. Mech. Anal.*, **118**, 71 (1992).
25. M. Gunzburger, *Finite-Element Methods for Viscous Incompressible Flows*, Academic Press, London, 1989.
26. D. E. Potter and G. H. Tuttle, 'The construction of discrete orthogonal coordinates', *J. Comput. Phys.*, **13**, 483 (1973).
27. S. B. Pope, 'The calculation of turbulent recirculatory flows in general orthogonal coordinates', *J. Comput. Phys.*, **26**, 197 (1978).
28. P. Morice, 'Numerical generation of boundary-fitted coordinate systems with optimal control of orthogonality, in K. N. Ghia and U. Ghia (eds.), *Advances in Grid Generation, FED-Vol. 5*, ASME Applied Mechanics, Bioengineering and Fluids Engineering Conference, Houston, 1983, p. 71.
29. W. G. Pritchard, P. Saavedra, L. R. Scott and S. J. Tavener, 'Asymptotic and numerical methods for approximating flows with a free boundary', preprint.
30. K. J. Ruschak, 'A method for incorporating free boundaries with surface tension in finite element fluid-flow simulators', *Int. j. numer. methods eng.*, **15**, 639 (1980).
31. N. P. Kruyt, C. Cuvelier, A. Segal and J. van der Zanden, 'A total linearization method for solving viscous free boundary flow problems by the finite element method', *Int. j. numer. methods fluids*, **8**, 351 (1988).
32. K. A. Cliffe, C. P. Jackson and A. C. Greenfield, 'Finite-element solutions for flow in a symmetric channel with a smooth expansion', *Harwell Report AERE R10608*, 1982.